A. Mannarino, E.H. Dowell
Reduced-Order Models for Computational-Fluid-Dynamics-Based Nonlinear Aeroelastic Problems
AIAA Journal, Vol. 53, N. 9, 2015, p. 2671-2685
doi:10.2514/1.J053775

Reduced order models for CFD-based, nonlinear aeroelastic problems

Andrea Mannarino*, Earl H. Dowell†

In this work, a nonlinear, state-space based identification method is proposed to describe compactly unsteady aerodynamic responses.
Such a reduced order model is trained on a series of signals which implicitly represent the relationship between the structural motion and the aerodynamic loads. The determination of the model parameters is obtained through a two-level training procedure, whereas in the first stage the matrices associated to the linear part of the model are computed by a robust subspace projection technique, while the remaining nonlinear terms are determined by an output error minimization procedure in the second stage.
The present approach is tested on two different problems, proving the convergence towards the reference results obtained by a computational fluid dynamics solver in linear and nonlinear, aerodynamic and aeroelastic applications, whereas the aerodynamic reduced order models are coupled with the related structural mechanical systems, demonstrating the ability of capturing the main nonlinear features of the response.
The robustness of the reduced order model is then tested considering a series of inputs with varying amplitude and frequency outside the range of interest and computing aeroelastic responses with non-null pre-twist angles.

Nomenclature

$\mathbf{x}_\mathrm{a}$	Aerodynamic state
$\mathbf{x}_\mathrm{s}$	Structural dynamics state
$\mathbf{A}_\mathrm{a}$, $\mathbf{B}_\mathrm{a}$, $\mathbf{C}_\mathrm{a}$, $\mathbf{D}_\mathrm{a}$	Linear sub-part of the reduced order model
$\mathbf{E}_\mathrm{a}$, $\mathbf{F}_\mathrm{a}$	Nonlinear sub-part of the reduced order model
$\boldsymbol{\phi}(\mathbf{x}_\mathrm{a})$	Nonlinear functions of the aerodynamic reduced order model

*Ph.D. Candidate, Dipartimento di Scienze e Tecnologie Aerospaziali, Politecnico di Milano, Via La Masa 34, 20156 Milano, Italy. Student member AIAA.
†William Holland Hall Professor, Department of Mechanical Engineering and Materials Science; Dean Emeritus, Pratt School of Engineering, Duke University, Durham, North Carolina 27708-0300. Honorary Fellow AIAA.

$\mathbf{f}_\mathrm{a}$	Aerodynamic loads
$q_\infty = \frac{1}{2}\rho_\infty U_\infty^2$	Dynamic pressure
h, θ	Plunge and pitch degree-of-freedom
β_LE, β_TE	Leading and trailing edge control surfaces deflection
N_a	Number of aerodynamic states, size of $\mathbf{x}_\mathrm{a}$
N_out	Number of aerodynamic output, size of $\mathbf{f}_\mathrm{a}$
b	Half chord, c/2
ω_i	Natural frequency of the i-th degree of freedom
$V = \frac{U_\infty}{\omega_\theta b\sqrt{\mu}}$	Reduced velocity
$\mu = \frac{m}{\pi\rho_\infty b}$	Mass-to-fluid ratio
t	Continuous time
$\tau = \omega_\theta t$	Non-dimensional time
$k = \frac{\omega\, c}{U_\infty}$	Reduced frequency
V_bif	Bifurcation speed

I. Introduction

Recently, reduced order models have been gaining more and more relevance in different branches of computational physics. The ability of capturing the main features of complex phenomena making use of a small number of degrees of freedom is particularly appealing in time critical applications. Aerospace industry may as well benefit from this kind of approach. Within this context, Computational Fluid Dynamics (CFD) is probably the most reliable tool for evaluating aerodynamic loads in the transonic regime during preliminary or even conceptual design stages of an aircraft. Even with the impressive improvements of modern computational methods, these computations are still too slow to be employed in industrial analyses, where sensitivity calculations and control law designs must be carried out for a large number of configurations. The situation is even more challenging when the interaction between structural flexibility and aerodynamic loads is taken into account, leading to aeroelastic models and dynamic response calculations. In this case, a wide spectrum of phenomena could be of interest, i.e. identification of the flutter point and evaluation of eventual limit cycle oscillations.

It is therefore of great importance to develop Reduced Order Models (ROM) from high fidelity numerical schemes to permit the use of nonlinear aerodynamics in a far wider analysis and design spectrum, while maintaining a reasonable level of accuracy. Reduced order models are not only encountered in aerodynamics,

in fact they are of great interest also in electromechanics [1, 2]. In structural dynamics such a concept is relatively old, used for many purposes ranging from the design of a test-analysis model to provide a basis for comparing computational and experimental results, to the alleviation of the computational burden associated with large-scale finite element models [3].

In the last decade, a significant effort has been directed toward developing compact models of transonic aerodynamics and computational aeroelastic problems [4, 5, 6]. Those ROMs must be able to capture the main features of the nonlinear problem under consideration, while maintaining a limited number of degrees of freedom. In the aeroelastic community, the most popular approaches include Proper Orthogonal Decomposition (POD) [5, 7], Harmonic Balance (HB) [6], generalized interpolation methods, e.g. Radial Basis Function (RBF) or Kriging interpolators [8, 9], Volterra theory [10, 11] and Neural Networks (NN), both static [12] and dynamic [13, 14].

The above listed methods tackle the problem of model order reduction in different ways. For example, POD and HB can be considered as subspace projection methods. In particular POD is useful when there is the need of reconstructing the flow variables in several locations inside the computational domain, while a huge amount of information would be wasted if only the estimation of the aerodynamic loads is of interest. On the other hand, HB is particularly efficient in the computation of periodic solutions, but its application range has not been extended to the evaluation of random or transient responses as yet. RBF and Kriging interpolators have been mainly employed for evaluating the stability boundary of aeroelastic systems when CFD-based aerodynamics is considered [8, 9]. They have proved to be quite versatile in unsteady aerodynamic predictions as well [15]. Concluding this brief review, Volterra and NN can be classified as identification methods: trained upon simple input-output data sets, they do not require any kind of special integration with CFD software. Volterra series have shown some difficulties in the identification of higher order kernels [4, 10, 16], while NN tackle the identification problem in an implicit nonlinear way, without taking into account any linear contribution. This fact could introduce modeling errors, especially in the estimation of the system bifurcation point.

The method that will be presented in the following sections will follow a NN-based approach [14], though structuring the aerodynamic model equations as a combination of linear and nonlinear contributions. In this way, the linear part will be mainly responsible for the estimation of the system bifurcation point, while the nonlinear terms will shape limit cycle oscillations beyond such a critical point. Instead of using a brute force identification of the aerodynamic loads, the proposed approach permits an improved physical understanding of the considered problem, as well as being a generalized reduced order modeling technique, applicable to a broad range of unsteady problems in computational physics. Also the training phase is different from the one discussed in Ref. [14], with the present approach that leads to a faster generation of reduced order models

than the technique detailed in Ref. [14], while maintaining a good level of accuracy.

The present work has multiple goals: present a novel, physics-based ROM technique, evaluate the importance of a correct training signal in the nonlinear domain, and finally perform convergence analyses in both aerodynamic and aeroelastic applications to determine the ROM sensitivity to parameter changes.

II. Reduced Order Modeling

The proposed identification technique is here directly applied to a generalized aerodynamic problem, however the same approach can be followed in several branches of physics. Furthermore, the data source on which the model will be trained may be generated in different ways. In this case only CFD-based results will be analyzed, but experimental data could also be employed as a training signal. Using the following identification-like approach, it is possible to structure the dynamic equations of the reduced order model in any way the analyst would prefer. We here present the following model:

$$\begin{cases} \dot{\mathbf{x}}_\mathrm{a} & = \mathbf{A}_\mathrm{a}\mathbf{x}_\mathrm{a} + \mathbf{B}_\mathrm{a}\mathbf{x}_\mathrm{s} + \mathbf{E}_\mathrm{a}\boldsymbol{\phi}\left(\mathbf{x}_\mathrm{a}\right) \\ \mathbf{f}_\mathrm{a}/q_\infty & = \mathbf{C}_\mathrm{a}\mathbf{x}_\mathrm{a} + \mathbf{D}_\mathrm{a}\mathbf{x}_\mathrm{s} + \mathbf{F}_\mathrm{a}\boldsymbol{\phi}\left(\mathbf{x}_\mathrm{a}\right) \end{cases} \tag{1}$$

where $\mathbf{x}_\mathrm{a}$ and $\mathbf{x}_\mathrm{s}$ are the aerodynamic and structural dynamics state, $\mathbf{A}_\mathrm{a}, \mathbf{B}_\mathrm{a}, \mathbf{C}_\mathrm{a}, \mathbf{D}_\mathrm{a}, \mathbf{E}_\mathrm{a}, \mathbf{F}_\mathrm{a}$ are the ROM parameters, $\mathbf{f}_\mathrm{a}$ are the aerodynamic loads and q_∞ is the flight dynamic pressure. The vectors $\boldsymbol{\phi}\left(\mathbf{x}_\mathrm{a}\right)$ are the nonlinear contributions to the ROM dynamics, where each component is a hyperbolic tangent function of the input, i.e. $\phi_i\left(x_{\mathrm{a},i}\right) = \tanh\left(x_{\mathrm{a},i}\right)$. The dimension of the aerodynamic state will be referred as N_a. The problem is formulated in the continuous time domain in order to permit variations in the integration time step depending on the analysis under consideration. For example, the time discretization can be modified during the design of a control law where the effect of different sampling times on the closed-loop system may be of interest. Such a variable-time-step feature could also be exploited in the search for limit cycle oscillation solutions, as reported in [14]. Equation 1 represents a nonlinear model in state space form, where the input is the structural dynamics state $\mathbf{x}_\mathrm{s}$ while the output is the generalized aerodynamic load $\mathbf{f}_\mathrm{a}$. An aerodynamic state is introduced to represent the intrinsic memory of the dynamic model, and in general it does not have any particular physical meaning. Nonlinear functions like the one employed in this case have already proved their potential in system identification [17].

Note also the particular structure of Eq. 1, where the model is nonlinear in the aerodynamic state only, while it is linear with respect to the structural state. In this way we are not forcing the system to depend nonlinearly on the input, as a brute force NN approach would have done, instead we are taking into consideration the physics of the problem. In fact, after running several CFD-based aeroelastic simulations, it

has been noticed that in the transonic regime large amplitude limit cycle oscillations are induced by the large motion of the shock wave on the moving body. Therefore nonlinearities are introduced in the model even when a linear structural system is considered. This means that the basic nonlinear behavior is introduced by the aerodynamic system only, and this is the reason of the linear dependence on the structural state in Eq. 1.

Finally, we would also point out the versatility of the present reduced order model. Even if it will be here used for predicting nonlinear response due to fluid-structure interaction, its parameterization could also allow to represent other nonlinear aerodynamic phenomena, such as vortex shedding [18].

II.A. Reduced order model training

The matrix entries of Eq. 1 must be determined through an optimization procedure. Because of the dynamic behavior of the model, and since the problem is formulated in the continuous time domain, simple linear least square approaches cannot be used here [10, 19].

The training of the reduced order model is tackled in two main stages. The first identifies the linear sub-part, i.e. matrices $\mathbf{A}_\mathrm{a}$, $\mathbf{B}_\mathrm{a}$, $\mathbf{C}_\mathrm{a}$, $\mathbf{D}_\mathrm{a}$, with a classical linear subspace projection technique [20]. The second stage of the training refines the reduced order model response by adding the nonlinear terms to the optimization procedure, i.e. matrices $\mathbf{E}_\mathrm{a}$ and $\mathbf{F}_\mathrm{a}$. Because of the intrinsic nonlinearity of the model, a generalized optimization method, such as the Levenberg-Marquardt (LM) [21] method is employed.

We remark that once the linear sub-model is trained, the nonlinear optimization will change only the terms related to the nonlinear part. Note however that these terms will contribute to the system linearization around the origin, modifying the eigenvalues between the first and second training stage. Therefore, from a rigorous mathematical viewpoint, we are not allowed to state that the linear and nonlinear phases are separated. This could be achieved considering nonlinearities of the type $\tanh(x) - x$, which present a null contribution at the origin when they are linearized. This approach is currently under the authors' consideration, but will not be pursued here. Nevertheless, after running several ROM trainings, it has been noticed that the most critical eigenvalues, i.e. the ones closest to the origin, remain substantially unchanged between the two training stages. Greater variations are experienced away from the origin, but without influencing the behavior of the linearized system to any substantial degree between the two phases, especially in the identification of the bifurcation point, as will be seen in Section III.C.

Thus dynamic linearized analyses can be performed right after the first part of the training, while the nonlinear contribution will mainly change the higher frequency eigenvalues, i.e. the ones farthest from the origin, improving the response fidelity.

As a first step, the training signal is generated by means of a CFD code. The type of training signal

chosen in our simulations will be detailed in the next section, but the proposed procedure would be able to treat signals generated by experimental data as well. Such a signal is made up by input-output data pairs, where the input is the structural motion while the output are the aerodynamic loads, and it is given as input to the following linear model:

$$\begin{cases} \dot{\mathbf{x}}_{\mathrm{a}} & = \mathbf{A}_{\mathrm{a}}\mathbf{x}_{\mathrm{a}} + \mathbf{B}_{\mathrm{a}}\mathbf{x}_{\mathrm{s}} \\ \mathbf{f}_{\mathrm{a}}/q_{\infty} & = \mathbf{C}_{\mathrm{a}}\mathbf{x}_{\mathrm{a}} + \mathbf{D}_{\mathrm{a}}\mathbf{x}_{\mathrm{s}} \end{cases} \tag{2}$$

This training phase makes use of a subspace projection technique to determine the matrices. The algorithm determines state sequences $\mathbf{x}_{\mathrm{a}}$ through the projection of input and output data, $\mathbf{x}_{\mathrm{s}}$ and $\mathbf{f}_{\mathrm{a}}/q_{\infty}$ respectively. These state sequences are outputs of non-steady state Kalman filter banks applied in parallel to the training data. From these results it is possible to determine the state space system matrices. Such an algorithm has proved to be always convergent (non-iterative) and numerically stable since it only makes use of QR algorithm and Singular Value Decompositions, as reported in Ref. [20].

The second stage of the training introduces the nonlinear terms. Because of the intrinsic nonlinear formulation of the model, a classical linear identification method cannot be employed. In this case, we employ the LM method to determine the entries of the matrices multiplying the nonlinear terms, but another optimization approach could have been used. Collecting the entries of the matrices $\mathbf{E}_{\mathrm{a}}$ and $\mathbf{F}_{\mathrm{a}}$ in a single, unknown vector $\mathbf{p}$, the following system of ordinary differential equations must be solved until the output error $\mathbf{e}(t) = \mathbf{f}_{\mathrm{a}}^{\mathrm{CFD}}(t) - \mathbf{f}_{\mathrm{a}}(t;\mathbf{p})$ is arbitrarily small:

$$\begin{cases} \dot{\mathbf{x}}_{\mathrm{a}} & = \mathbf{A}_{\mathrm{a}}\mathbf{x}_{\mathrm{a}} + \mathbf{B}_{\mathrm{a}}\mathbf{x}_{\mathrm{s}} + \mathbf{E}_{\mathrm{a}}\boldsymbol{\phi}(\mathbf{x}_{\mathrm{a}}) \\ \dot{\mathbf{x}}_{\mathrm{a}_{/\mathbf{p}}} & = \left(\mathbf{A}_{\mathrm{a}} + \mathbf{E}_{\mathrm{a}}\boldsymbol{\phi}(\mathbf{x}_{\mathrm{a}})_{/\mathbf{x}_a}\right)\mathbf{x}_{\mathrm{a}_{/\mathbf{p}}} + \mathbf{E}_{\mathrm{a}_{/\mathbf{p}}}\boldsymbol{\phi}(\mathbf{x}_{\mathrm{a}}) \\ \mathbf{f}_{\mathrm{a}}/q_{\infty} & = (\mathbf{C}_{\mathrm{a}}\mathbf{x}_{\mathrm{a}} + \mathbf{D}_{\mathrm{a}}\mathbf{x}_{\mathrm{s}} + \mathbf{F}_{\mathrm{a}}\boldsymbol{\phi}(\mathbf{x}_{\mathrm{a}})) \\ \mathbf{f}_{\mathrm{a}_{/\mathbf{p}}}/q_{\infty} & = \left(\mathbf{C}_{\mathrm{a}} + \mathbf{F}_{\mathrm{a}}\boldsymbol{\phi}(\mathbf{x}_{\mathrm{a}})_{/\mathbf{x}_a}\right)\mathbf{x}_{\mathrm{a}_{/\mathbf{p}}} + \mathbf{F}_{\mathrm{a}_{/\mathbf{p}}}\boldsymbol{\phi}(\mathbf{x}_{\mathrm{a}}) \end{cases} \tag{3}$$

Analytic expressions for the sensitivity terms $\mathbf{x}_{\mathrm{a}_{/\mathbf{p}}}$ and $\mathbf{f}_{\mathrm{a}_{/\mathbf{p}}}$ are provided in the Appendix. Stacking the

values of the computed $\mathbf{e}$ and $\mathbf{f}_{a_{/\mathbf{p}}}$ at each simulation time step t_i in the two following quantities:

$$\mathbf{g} = \begin{Bmatrix} \mathbf{e}(t_1) \\ \mathbf{e}(t_2) \\ \vdots \\ \mathbf{e}(t_i) \\ \vdots \\ \mathbf{e}(t_N) \end{Bmatrix} \qquad \mathbf{J} = \begin{bmatrix} \mathbf{e}_{/\mathbf{p}}(t_1) \\ \mathbf{e}_{/\mathbf{p}}(t_2) \\ \vdots \\ \mathbf{e}_{/\mathbf{p}}(t_i) \\ \vdots \\ \mathbf{e}_{/\mathbf{p}}(t_N) \end{bmatrix} = - \begin{bmatrix} \mathbf{f}_{a_{/\mathbf{p}}}(t_1) \\ \mathbf{f}_{a_{/\mathbf{p}}}(t_2) \\ \vdots \\ \mathbf{f}_{a_{/\mathbf{p}}}(t_i) \\ \vdots \\ \mathbf{f}_{a_{/\mathbf{p}}}(t_N) \end{bmatrix} \tag{4}$$

the vector $\mathbf{p}$ is updated at each iteration through the solution of the following least-square problem:

$$\left(\mathbf{J}^{\mathrm{T}}\mathbf{J} + \lambda\mathbf{I}\right)(\mathbf{p}_{\mathrm{new}} - \mathbf{p}_{\mathrm{old}}) = -\mathbf{J}^{\mathrm{T}}\mathbf{g} \tag{5}$$

being λ a regularization parameter, usually very small, used to keep the left hand side matrix always non-singular [21]. The same training signal is presented to Eq. 3 at each optimization iteration, the time histories of $\mathbf{x}_a$ and $\mathbf{f}_a$ are computed, and the value of $\mathbf{p}$ is updated through Eq. 5. The iterations are stopped when a sufficiently small euclidean norm of the output error $||\mathbf{e}||_2$ is achieved or when the variation between two iterations is smaller than a user-defined threshold.

II.B. Training signals

The design of training signals in nonlinear identification problems is not as simple as its linear counterpart. In fact, it is not sufficient to excite the desired frequency range to obtain physically meaningful ROMs, but it is also necessary to perturb the system with signals with suitable amplitudes. Furthermore, the superposition principle cannot be applied in these cases. In order to overcome this obstacle, the problem must be tackled from a different prospective. From the linearized analysis, often available in preliminary design concepts, we may take advantage of knowledge of two very important parameters: the flutter frequency and the aeroelastic eigenmode at the flutter point.

The first parameter helps us to determine the frequency range to be excited by the training signal. As a matter of fact, at the generalized force level, aerodynamic nonlinearities are substantially smooth, e.g. they change the system properties in a regular way. The same cannot be said about the so called 'hard' nonlinearities, e.g. structural friction and free-play [22], which are able to switch the system behavior in a discontinuous manner. Taking this assumption as valid, the training signal is designed to excite a relatively broad frequency range, covering the critical frequencies of interest. Even in presence of 'hard' nonlinearities this approach would still be valid, taking care of broadening the signal frequency content. Also, signals

with a wide frequency content would be suitable in analyzing a large spectrum of responses, thus being particularly useful in control law designs.

The aeroelastic mode at the flutter point leads us to the determination of proper signal amplitudes. Fixing the amplitude of one degree of freedom, all the others are determined, since the eigenvector is defined. So, even running a coarse CFD-based simulation, or with a trial-and-error approach, the amplitude range for the training signal can be easily determined.

Finally, the type of training signal has to be chosen. Since the superposition principle is not valid, the system has to be simultaneously excited in all of its degrees of freedom. This has been verified through extensive simulations. Furthermore, in the authors' experience, step sequences and frequency sweep signals have not proven to be good excitations in the present applications. This is in contrast with the results obtained in [16, 23, 11], where Volterra series are used to predict unsteady responses of nonlinear CFD-based aerodynamic simulations. In the present case, random-like and noisy sweep signals have always produced physically meaningful ROMs, and this is in accordance with the results reported in [10]. It is the authors' opinion that to identify large amplitude limit cycle oscillations, a series of step and impulse functions is not adequate. This kind of signal would be useful in the identification of weak nonlinearities. In the present case, the moving shock wave undergoes very large displacements, eventually disappearing and reappearing during a cycle, as shown in Figure 1 in the case of an airfoil experiencing LCO. It is evident that when the shock on the upper surface reaches its maximum strength the one on the lower surface is absent, and vice versa. This kind of behavior can be captured better by the training signals used in this work. An example of this kind of signal is given in Fig. 2.

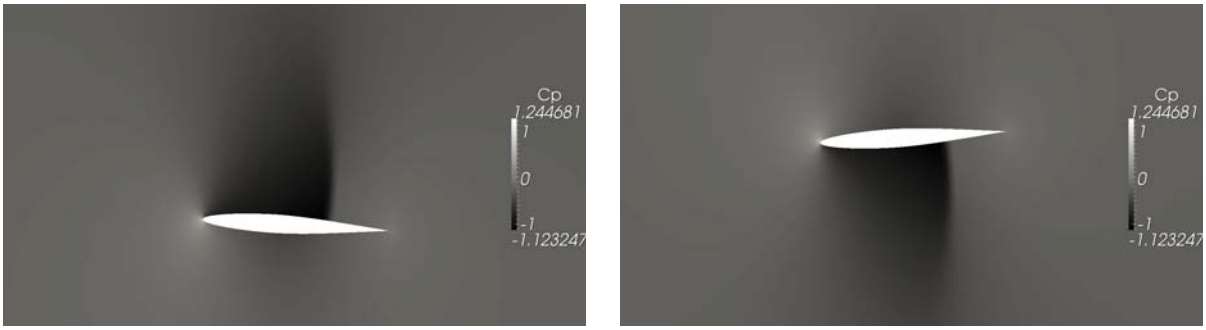

(a) Maximum aft position of the shock on the airfoil upper surface.

(b) Maximum aft position of the shock on the airfoil lower surface.

Figure 1: Oscillation of the shock wave during an LCO at $V = 0.775$.

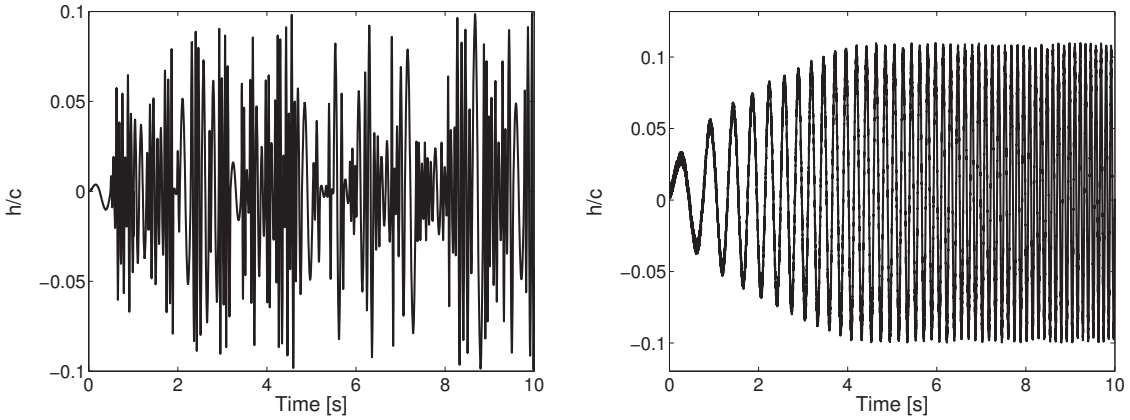

(a) Random-like signal **(b)** Disturbed sweep signal

Figure 2: Sample of training signals able to produce physically meaningful ROMs.

A detailed definition of these signals is provided here. The so called random-like signal is generated by first reproducing a white noise sequence with assigned root mean square and then a second order filter, of the type $G(s) = \dfrac{\omega_0^2}{s^2 + 2\xi\omega_0 s + \omega_0^2}$ is applied to it, with $\xi = 1$ and ω_0 dependent on the problem under consideration. The resulting signal is a smooth function of time which persistently excites the amplitude and frequency range of interest.

The noisy sweep signal is a classical frequency sweep signal disturbed in both amplitude and phase by a white noise with a small root mean square, defined by:

$$u(t) = (A + \mathrm{wgn}_A) \cdot \sin\left(\omega_i + \frac{\omega_f - \omega_i}{T} t + \phi + \mathrm{wgn}_\phi\right), \qquad t \leq T \tag{6}$$

Here A is the signal amplitude and wgn_A is the related disturbance, ω_i and ω_f are the initial and final frequency of the signal, T is the simulation time, ϕ is the signal phase and wgn_ϕ is the related disturbance. It might be thought that a signal similar to a limit cycle oscillation would help the ROM to identify this kind of behavior once coupled with a mechanical system. According to the results of this work, this is indeed the case, but only when such a signal contains a sufficient level of noise in amplitude and phase. In fact, it is found that a training signal which considers an input of harmonic oscillations from the aeroelastic LCOs leads to an erroneous identification of the system nonlinear behavior, always resulting in unbounded, unstable aeroelastic responses, as if the identified system is linear. Thus a random-like signal is selected in the following analyses. The excited frequencies and amplitudes can be chosen a priori, selecting the lower and upper values of the frequency range and the root mean square of the signal. Furthermore, using a white noise based signal we are assured that the time history of the various input channels will not be correlated, as shown in Figure 3, increasing the chances of obtaining meaningful identification results.

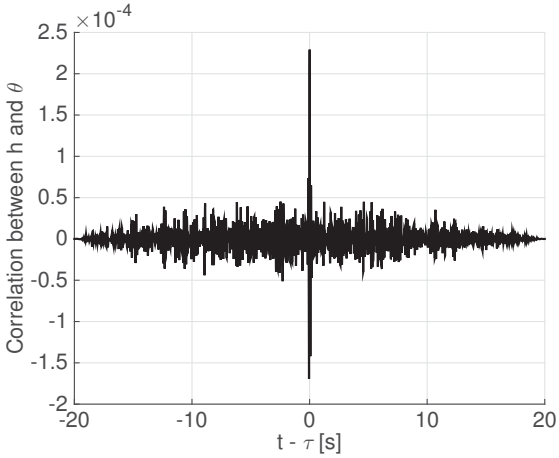

Figure 3: Cross correlation between plunge and pitch training signals in the two degree-of-freedom case.

III. Sample Applications

III.A. Aerodynamic solver

The aerodynamic sub-system is modeled by a cell centered finite volume scheme, using the aerodynamic code AeroFoam, developed at Dipartimento di Scienze e Tecnologie Aerospaziali, Politecnico di Milano [24]. AeroFoam is a density-based compressible Unsteady Euler/Reynolds-Averaged-Navier-Stokes solver, the Euler option being selected in this work. Among its features there is an aeroelastic interfacing scheme, based on a moving least square interpolation strategy, providing all the needed functionalities to set the appropriate aerodynamic boundary conditions imposed by a deforming structure, while driving a connected hierarchical mesh deformation within an Arbitrary Lagrangian Eulerian formulation. An extended discussion of its aeroelastic capabilities can be found in [25].

III.B. Test case

The previously presented technique is here applied to a plunging and pitching NACA 0012 airfoil, flying at $M_\infty = 0.8$ in air. The airfoil is equipped with two movable control surfaces, at the leading and trailing edge, with the two hinges placed at 15% and 75% chord respectively. A schematic representation of the system is depicted in Fig. 4. The same structural model is employed in the following two examples, where at first the control surfaces are held fixed, reducing the number of structural degrees of freedom to two, while in the second case all of the airfoil parts are left free to move.

The computational meshes used in CFD calculations are depicted in Fig. 5. After a convergence analysis based on static aerodynamic data, the C-type topology mesh around the airfoil is discretized with 30000 elements in the case of the two degree-of-freedom model, as shown in Fig. 5a. Regarding the four degree-of-freedom case instead, the mesh around the airfoil is discretized with 32000 elements, increasing the cell

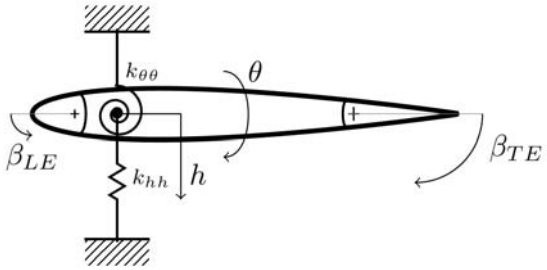

Figure 4: Typical section.

density near the control surfaces hinges, in order to track the local surface motion with higher accuracy, as shown in Fig. 5b. The system of ordinary differential equations governing the dynamics of the aeroelastic

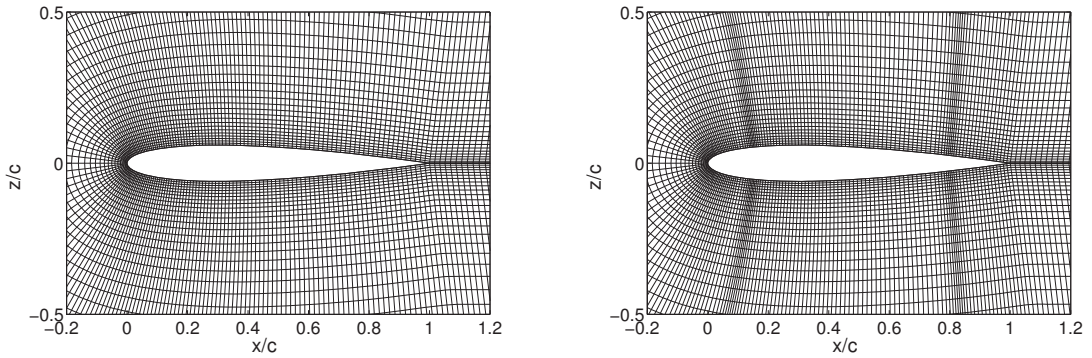

(a) Two degree-of-freedom model - mesh close-up. **(b)** Four degree-of-freedom model - mesh close-up.

Figure 5: Different meshes used in CFD calculations.

system is given in Eq. 7, while the structural parameters are reported in Table 1.

$$\begin{bmatrix} 1 & x_\theta & x_{\beta_{\mathrm{LE}}} & x_{\beta_{\mathrm{TE}}} \\ x_\theta & r_\theta^2 & j_{\beta_{\mathrm{LE}}}^2 & j_{\beta_{\mathrm{TE}}}^2 \\ x_{\beta_{\mathrm{LE}}} & j_{\beta_{\mathrm{LE}}}^2 & r_{\beta_{\mathrm{LE}}}^2 & 0 \\ x_{\beta_{\mathrm{TE}}} & j_{\beta_{\mathrm{TE}}}^2 & 0 & r_{\beta_{\mathrm{TE}}}^2 \end{bmatrix} \begin{pmatrix} h_{\tau\tau}/b \\ \theta_{\tau\tau} \\ \beta_{\mathrm{LE},\tau\tau} \\ \beta_{\mathrm{TE},\tau\tau} \end{pmatrix} + \begin{bmatrix} (\omega_h/\omega_\theta)^2 & 0 & 0 & 0 \\ 0 & r_\theta^2 & 0 & 0 \\ 0 & 0 & (\omega_\beta/\omega_\theta)^2 & 0 \\ 0 & 0 & 0 & (\omega_\beta/\omega_\theta)^2 \end{bmatrix} \begin{pmatrix} h/b \\ \theta \\ \beta_{\mathrm{LE}} \\ \beta_{\mathrm{TE}} \end{pmatrix} = \frac{V^2}{\pi} \begin{pmatrix} -C_L(\tau) \\ 2\,C_M(\tau) \\ 2\,C_{M_{\beta_{\mathrm{LE}}}}(\tau) \\ 2\,C_{M_{\beta_{\mathrm{TE}}}}(\tau) \end{pmatrix} + \begin{bmatrix} 0 \\ r_\theta^2 \\ 0 \\ 0 \end{bmatrix} \theta_0 \tag{7}$$

The variable θ_0 in Eq. 7 represents the static pre-twist in the torsional spring and it will be used to test

x_θ	r_θ^2	ω_h/ω_θ	μ	$x_{\beta_{\mathrm{LE}}}$	$x_{\beta_{\mathrm{TE}}}$	$j_{\beta_{\mathrm{LE}}}$	$j_{\beta_{\mathrm{TE}}}$	$r_{\beta_{\mathrm{LE}}}^2$	$r_{\beta_{\mathrm{TE}}}^2$	$\omega_\beta/\omega_\theta$
0.25	0.75	0.5	75	0.0375	0.05	0	0	0.1125	0.15	3

Table 1: Structural parameters of the typical section.

the robustness of the computed ROM in conditions not considered during its training. The reduced velocity $V = U_\infty/(\omega_\theta b\sqrt{\mu})$ is the bifurcation parameter of the model: beyond a critical value, the linearized system

becomes unstable around the origin. Then, thanks to the nonlinearities introduced by the aerodynamics, the response will eventually converge on stable limit cycle oscillation trajectories.

III.C. Two degree-of-freedom typical section

Before generating the signals used to train the ROM, several CFD-based aeroelastic analyses have been carried out to better understand the physics behind the nonlinear behavior of this test case. It has been determined that LCOs are brought into the system due to the large motion of strong shock waves over the oscillating airfoil. The resulting oscillations increase in amplitude as the reduced velocity is increased, as shown in Fig. 6. This growth in amplitude can be explained by analyzing the length swept by the shock wave in one cycle, as reported in Fig. 7. As it can be seen, the chord length swept by the shock is always larger than 13%c, indicating that the aerodynamics are introducing strong nonlinear effects in the system. It is also clearly visible how the growth of the LCO amplitude depends almost linearly on the length swept by the shock wave. However even though these two variables are in linear proportion to each other, the aerodynamic loads are nonlinear functions of the LCO amplitude as is expected for a nonlinear system.

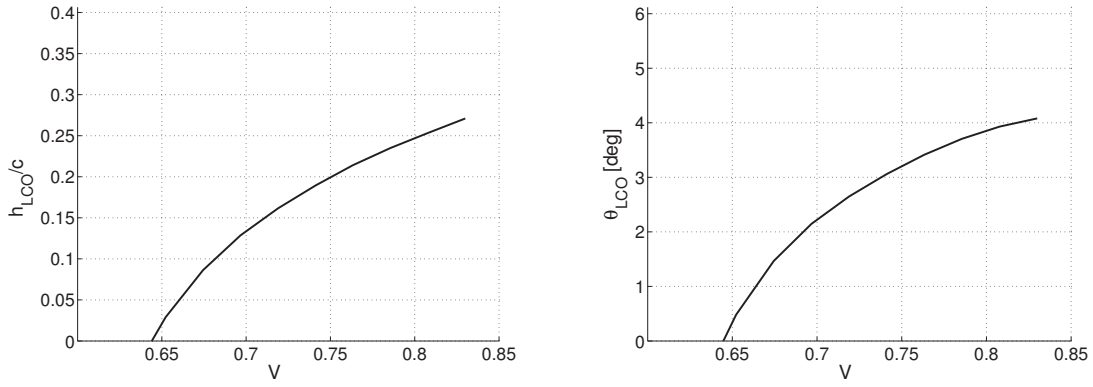

(a) Plunge trend. **(b)** Pitch trend.

Figure 6: LCO trends computed by CFD-based simulations.

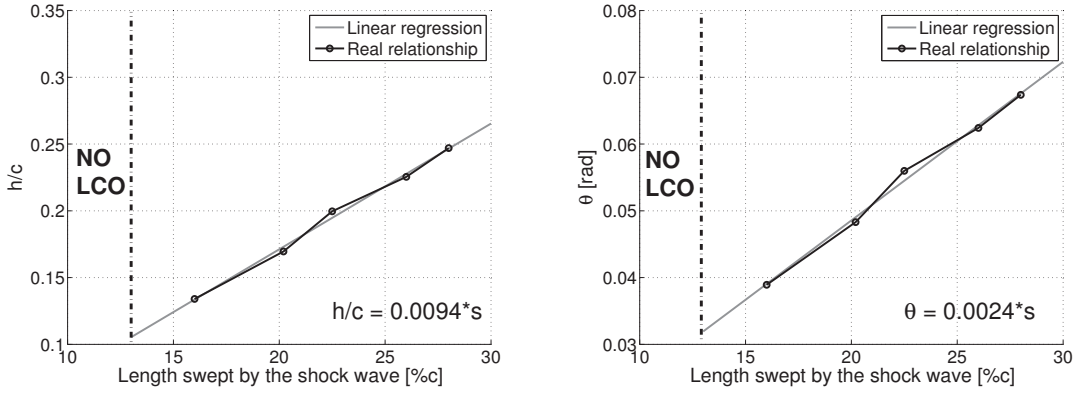

(a) Plunge dependence. **(b)** Pitch dependence.

Figure 7: Dependence of the LCO amplitude on the length swept by the shock wave.

Computing Fast Fourier Transforms of the obtained LCOs, it is then possible to analyze the variation of frequency with the reduced velocity, as depicted in Fig. 8. As it can be noticed, the LCO frequency remains confined in a narrow range, e.g. $k = 0.2 - 0.23$, so it may be assumed that a training signal designed to excite the aerodynamic system within such a frequency range will probably lead to a correct identification of this peculiar nonlinear behavior.

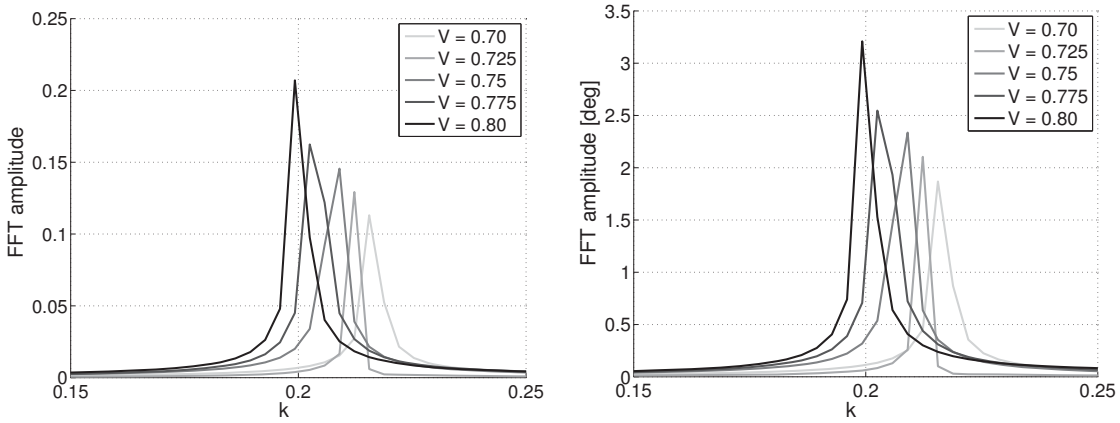

(a) Plunge frequency trend. **(b)** Pitch frequency trend.

Figure 8: LCO frequency trends computed by CFD-based simulations.

The time required to fully develop an LCO using standard CFD time marching methods is about 8 hours on 4 Intel® Core™ i5-3470 CPU units running at 3.2 GHz on a desktop workstation. All the simulations are run with a physical time step $\Delta t_{\text{CFD}} = 10^{-3}$ seconds, using a 5th order accurate Runge-Kutta scheme. The convergence between time steps is accelerated by multigrid and dual time stepping methods.

A training signal can now be designed based on the information collected through the preliminary analyses. The input-output pair used in the training stage is shown in Fig. 9. A zoom of the same signal near its end is presented in Figure 10 to show its smooth behavior. It covers a broad frequency spectrum, as reported

in Fig. 11a. The structural motion used as training input has a ratio $h/(c\theta) = 3.5$, and, as shown in Fig. 11b, this ratio remains almost constant in a wide range of flight speeds. The training signal is generated by

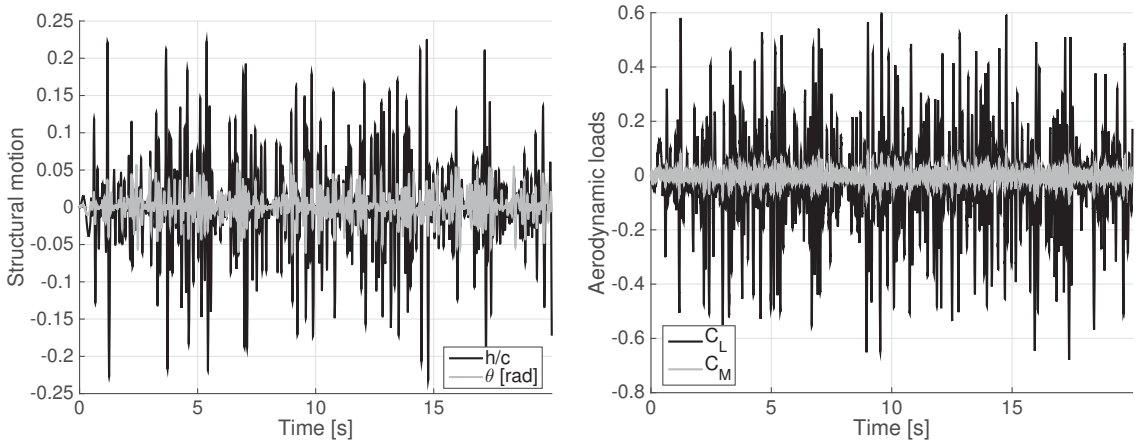

(a) Input: structural motion. **(b)** Output: aerodynamic loads.

Figure 9: Training signal.

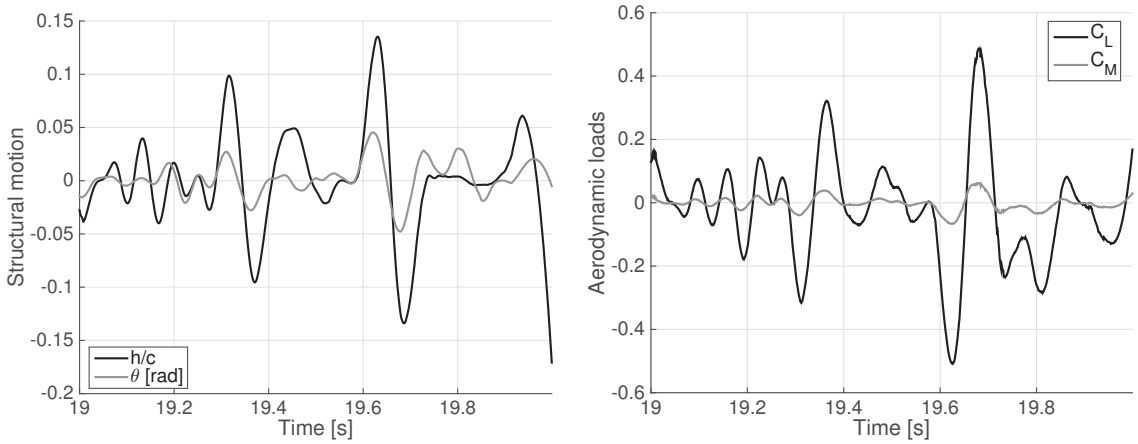

(a) Input: structural motion. **(b)** Output: aerodynamic loads.

Figure 10: Close-up near the training signal end.

the structural motion depicted in Fig. 9a prescribed to the CFD solver, which computes the load history of Fig. 9b. The root mean square of the plunge and pitch degrees of freedom is set to 0.15 and 0.045 radians respectively, while the parameter ω_0 of the smoothing filter is set to obtain a cut-off reduced frequency of $k = 0.4$. The resulting signal is quite long in length (20 seconds) and it is used to perform a ROM convergence analysis. Several training periods are carried out considering different time intervals of the same signal, requiring only one reference signal, and obtaining the required results in about 10 hours. Series of ROMs are then computed considering an increasing number of aerodynamic states N_a, from 5 to 12, and various training signal time intervals: 5, 10, 15 and 20 seconds. Such a convergence analysis is carried out assuming as a target value the bifurcation velocity of the system, usually available from linearized analyses. In this case instead such a value has been extrapolated from CFD analyses, resulting in $V_{\text{bif}} = 0.64$. In

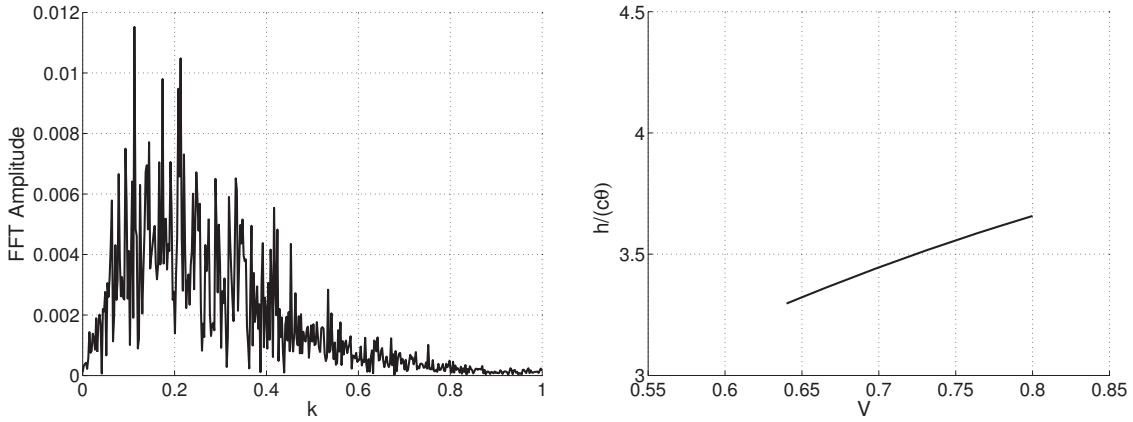

(a) Fast Fourier transform of the plunge training signal. **(b)** LCO amplitude ratio.

Figure 11: Frequency and amplitude characteristics of the training signal.

Fig. 12a is presented the convergence analysis performed on this test case. It is evident that as the length of the training signal is increased, the convergence towards the reference value becomes smoother. For signals longer than 5 seconds the results are very similar for a number of aerodynamic states greater than 10. In Fig. 12b instead it is shown the time required to train a ROM on the different training signals. Notice that the ROM training is performed on a single CPU of the previously mentioned workstation. The maximum number of iterations allowed to the LM algorithm is limited to 50, with a converged cost function threshold value set at 10^{-3}. Both the input and the output have been normalized by their maximum value, to appropriately weigh the fitting errors. A reasonably good trade-off between accuracy and computational time required is achieved by ROMs trained on the 10 second long signal. The comparison between the CFD and these ROM-based results is depicted in Fig. 13. It can be seen that a reasonable match between the two methods is obtained for a number of states $N_a > 10$. The best bifurcation point estimation is obtained by the ROM with $N_a = 12$, which predicts $V_{\text{bif}} = 0.635$. Considering only the linear part of the same model, the computed bifurcation speed is $V_{\text{bif}} = 0.629$, therefore proving that the assumptions of Section II.A are valid in this case. After a convergence analysis, a number of states equal to $n_x = 4$ and a number of hidden neurons equal to $n_h = 8$ have proven to be adequate in LCO predictions. For the details please see [14]. As can be seen, this ROM produces accurate LCO amplitude trends. Finally, in Fig. 14 is shown the comparison between the LCO frequency trends. Once again the ROM proves to be quite accurate in the prediction of the LCO main features. The results obtained by the ROM of ref. [14] are almost identical. All the ROM-based simulations are performed using an implicit, L-stable time integration method, with tunable numerical dissipation [27], run with a time step $\Delta t_{\text{ROM}} = 10 \cdot \Delta t_{\text{CFD}}$, demonstrating the robustness of the proposed approach considering variations of the time discretization. In conclusion to this analysis, in Table 2 is reported a comparison of the time required to compute the LCO trends depicted in Fig. 13. According to the obtained results, the time savings is substantial. What would take a CFD model an hour

to calculate, the ROM can do in 0.7 seconds, maintaining a reasonable accuracy. As can be noticed, the ROM of ref. [14] requires a longer training time, and this is due to the training approach used in that case, composed always by two stages but made up by a genetic algorithm and the LM method, because of the implicit nonlinear parameterization of the system [14]. Therefore, in comparison with the one of ref. [14], the ROM here presented is computed in a shorter time and permits the analyst to parameterize the system in a much simpler way.

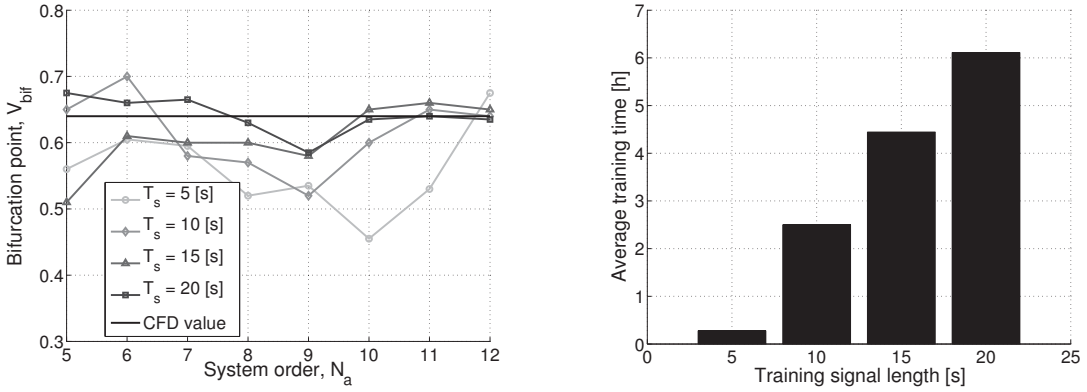

(a) Convergence analysis based on the bifurcation point. **(b)** Time required for the training.

Figure 12: Convergence analysis for the two degree-of-freedom airfoil.

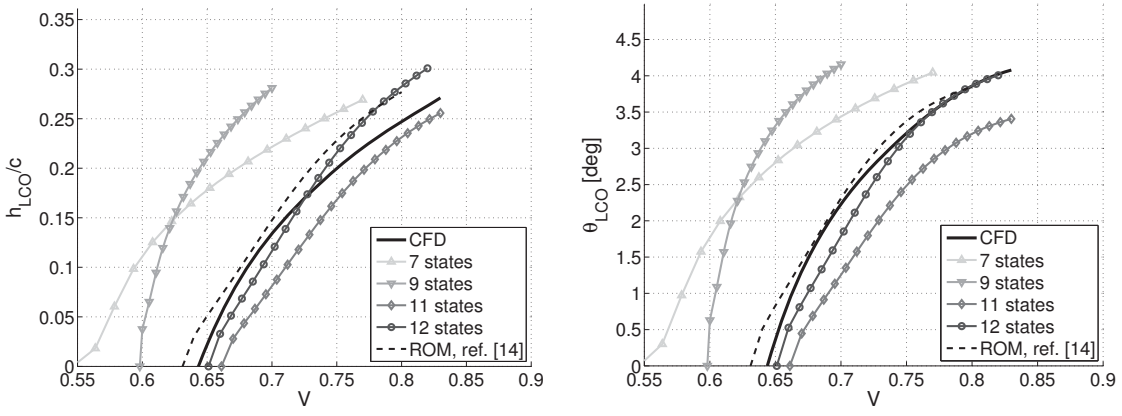

(a) Plunge trend. **(b)** Pitch trend.

Figure 13: Comparison of LCO amplitude trends. The training signal considered is 10 seconds long.

In order to test the ROM robustness in aeroelastic applications, a non-null pre-twist pitch angle θ_0 is now considered. The computation of LCO trends is performed at $\theta_0 = 1$ deg and $\theta_0 = 2$ deg. Given that the maximum LCO pitch angle experienced in the null pre-twist case was equal to 4 degrees, the computation of aeroelastic responses with these new pre-twist values means that we are considering new perturbed conditions, with perturbations of 25% and 50% respectively, with respect to the nominal condition for which the ROM was originally computed. The results relative to $\theta_0 = 1$ deg are shown in Figure 15, while the ones obtained with $\theta_0 = 2$ deg are presented in Figure 16. Notice that the variables are now $\Delta h/c$ and $\Delta\theta$, computed as

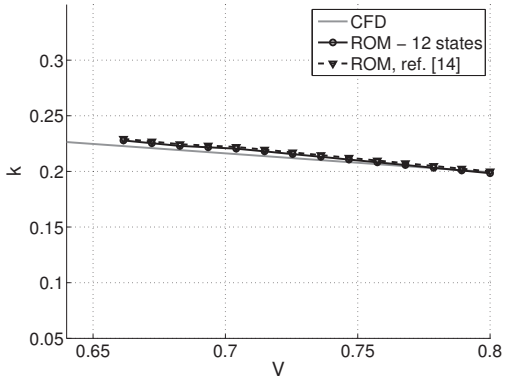

Figure 14: Comparison of LCO frequency trend. The training signal considered is 10 seconds long.

	CFD	ROM	ROM, ref. [14]
Training signal generation, hours	-	10	10
Training stage, hours	-	2.5	4
Trend calculation, hours	8×8 points	0.0015×22 points	0.0012×22 points
	64	0.033	0.0264
Total, hours	64	12.533	14.0264

Table 2: Computational time required for computing the LCO trends, 2 degree-of-freedom typical section.

$[\max(\text{LCO}) - \min(\text{LCO})]/2$, because the LCOs are no longer symmetric in this case.

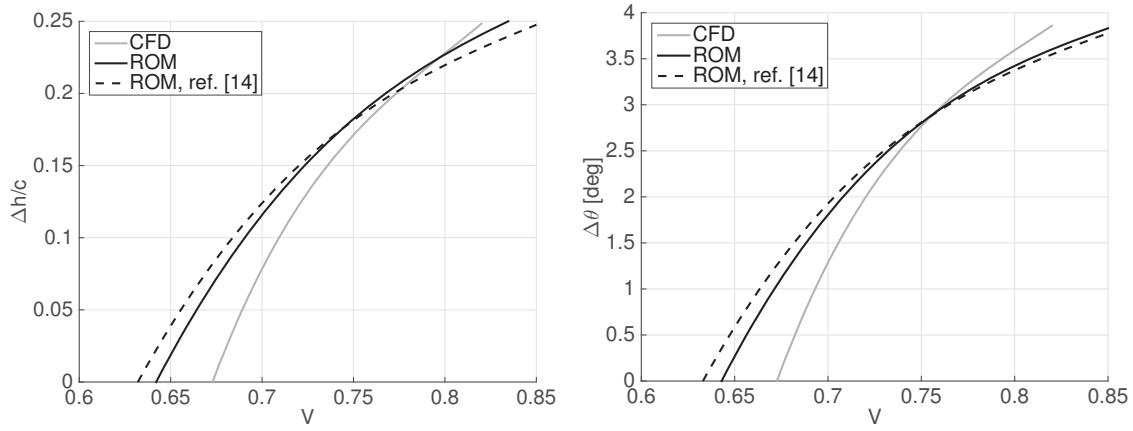

(a) Plunge trend. **(b)** Pitch trend.

Figure 15: Comparison of LCO amplitude trends. Pre-twist angle of 1 deg.

Good results, comparable with the $\theta_0 = 0$ deg case are obtained for $\theta_0 = 1$ deg. The amplitude trend is tracked with a good accuracy by the ROM with $N_a = 12$. Similar results are obtained with the ROM of ref. [14]. Unfortunately, the same cannot be said for the case $\theta_0 = 2$ deg where the amplitude trend changes dramatically in shape, resulting in an unstable LCO behavior [26], probably because of the strong influence of the pre-twist angle. The ROM produces an LCO trend similar to the previous cases, being not able to

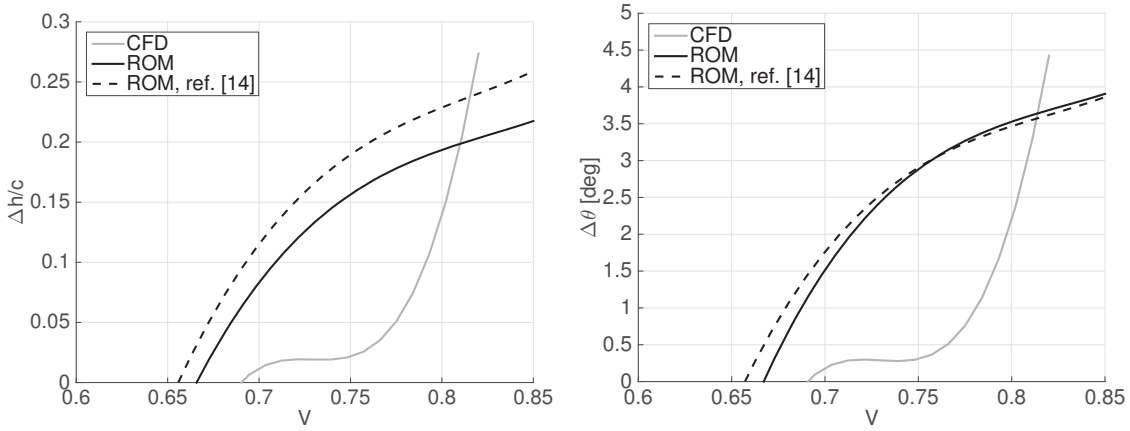

(a) Plunge trend. **(b)** Pitch trend.

Figure 16: Comparison of LCO amplitude trends. Pre-twist angle of 2 deg.

change its behavior. Qualitatively, the same results are obtained by the ROM of ref. [14]. A possible solution to this problem could be a new training which takes into account a non-null mean pitch angle, but this is beyond the scope of the present analysis, and will not be pursued here. In conclusion, it can be stated that the ROM presents good robustness features around the nominal condition for which it has been trained, producing accurate results at least up to a 25% perturbation in the pre-twist angle.

In addition to these analyses, it is worth noting that as a reduced order aeroelastic model has been tested so far, a reduced order aerodynamic model is available as well. So, if the analyst is not only interested in evaluating nonlinear aeroelastic responses, but also in computing unsteady aerodynamic loads given a prescribed motion, the proposed ROM is able to perform this task.

First of all, in Section II.A, the behavior of the system eigenstructure between the two training stages has been discussed, stating that the eigenvalues of the aerodynamic system do not change dramatically during the training. Even if this fact cannot be predicted analytically, the results of this work confirm this assumption, as witnessed by Figure 17 in the case $N_a = 12$ and $T_s = 10$ s. As can be noticed, the eigenvalues are indeed modified during the two phases, but the ones near the imaginary axis remain almost unchanged, as shown by Figure 17b. Therefore, the stability properties of the system are conserved. This result supports the conclusion that the linear sub-part of the aerodynamic ROM, composed by the matrices $\mathbf{A}_a$, $\mathbf{B}_a$, $\mathbf{C}_a$ and $\mathbf{D}_a$ resulting from the first stage of the training, is a good approximation of the aerodynamic system for small input, as the structural modes will interact predominantly with the aerodynamic modes closest to the origin.

It is shown here that the ROM presents a good performance in the identification of unsteady aerodynamic loads over a broad range of input frequencies and amplitude ratios. Several analyses have been carried out, and the most interesting findings of this campaign are here presented. At first, the aerodynamic ROM is excited by an harmonic input with small amplitude in both plunge and pitch degrees of freedom. The motion

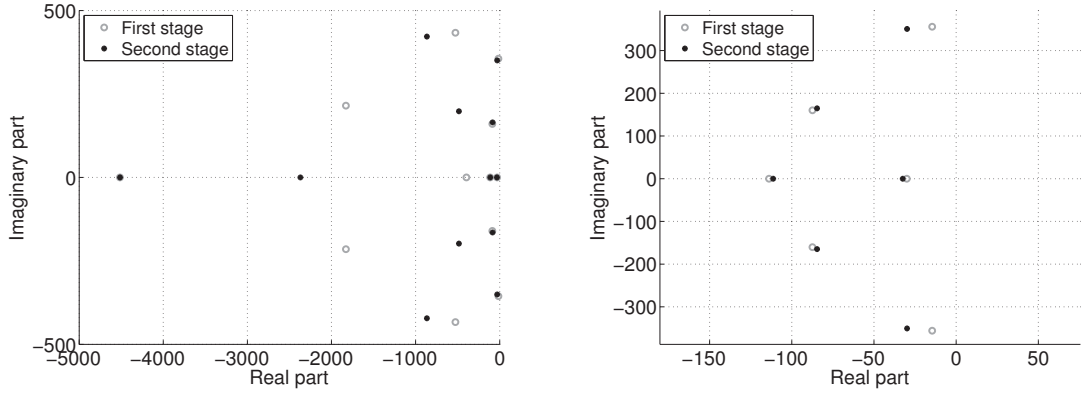

(a) Root locus. **(b)** Close-up near the origin.

Figure 17: Eigenvalues of the aerodynamic system between the two training phases.

amplitude is set to $\bar{h}/c = 0.01$ for the plunge and $\bar{\theta} = 0.1$ deg for the pitch. The excitation reduced frequency is set to $k = 0.6$, which is not well excited by the training signal used before, as shown in Figure 11a. The computational time required for simulating 1.5 seconds of physical time by the present CFD solver is in this case equal to 20 minutes. The ROM is able to compute the same response in a few seconds. This test is performed to assess the ROM performance for small input perturbations only, comparing the variation of the predicted results between the two training stages. The results in terms of lift and moment coefficients are presented in Figure 18, showing a close-up near the FFT peak. As it can be noticed from Figure 18a, very good results, almost identical, are obtained by both linear (one training stage only) and nonlinear ROMs in the prediction of the lift coefficient. The same accuracy is obtained for the moment coefficient, as shown in Figure 18b. In this case however, some differences can be distinguished between the different ROMs. Even though they all present almost the same accuracy, the nonlinear ROM with $N_a = 12$ is the one closest to the reference response, while the others present a convergent behavior toward the reference CFD solution as the number of aerodynamic states is increased.

Two conclusions may be drawn from these results. First, both linear and nonlinear ROMs present good accuracy when the input amplitude is small enough to assume the aerodynamic system as linear. Second, the nonlinear ROM is always performing better than the linear ROM.

The nonlinear performance of the ROM is evaluated considering large amplitude structural input, always at the same frequency of the previous case. The motion amplitude is set to $\bar{h}/c = 0.3$ for the plunge and $\bar{\theta} = 5$ deg for the pitch degree of freedom, both much greater than the maximum amplitude excited by the training signal shown in Figure 9. In this case the attention is focused on the moment coefficient, because it is the one characterized by the strongest nonlinear behavior. The computational time required for simulating 1.5 seconds of physical time by the present CFD solver is about 3 hours. Thus, in this case the computational savings introduced by the ROM is substantial. The results are presented in Figure 19, with a close-up near

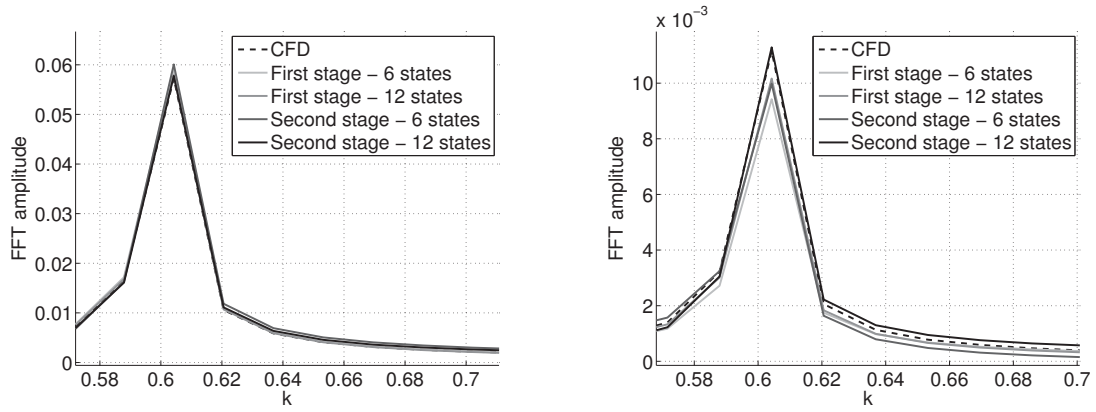

(a) Lift coefficient. **(b)** Moment coefficient.

Figure 18: Aerodynamic loads FFT for small structural motion.

the FFT peaks. It can be noticed that, as the number of states is increased, the ROM response gets closer to the reference solution, even if small differences are still present. This is due to an insufficient excitation of these input amplitudes during the training phase. Notice however that the refined ROM is able to replicate accurately the different harmonics in the response.

The robustness of the proposed ROM in both linear and nonlinear regimes demonstrates that reasonably accurate results can be obtained by the linear ROM also, taking care of operating with small structural input.

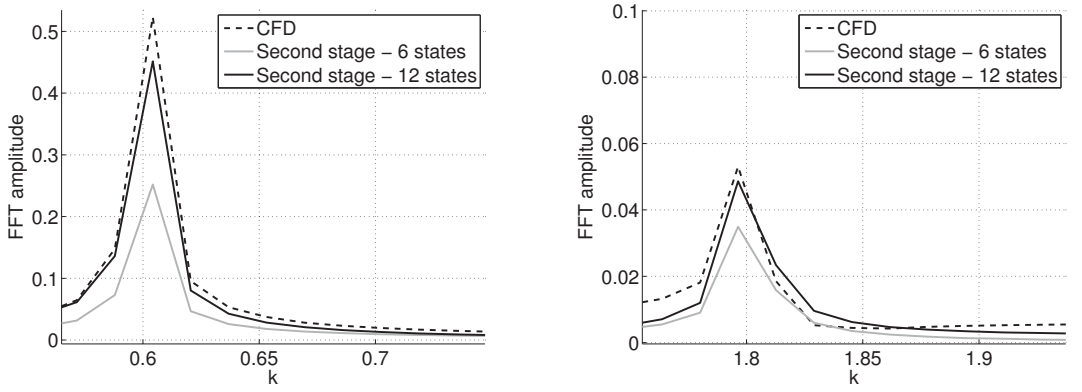

(a) Close-up near the first harmonic response peak. **(b)** Close-up near the third harmonic response peak.

Figure 19: Moment coefficient FFT for large structural motion, two degree-of-freedom case.

III.D. Four degree-of-freedom typical section

Even though very similar to the previous test case, this problem is presented to show the ability of the proposed ROM to deal with systems with a larger number of degrees of freedom, and to set the basis for a nonlinear aeroservoelastic benchmark. In fact, the control surfaces may be used to suppress the LCOs

[28, 29].

Assuming this case will present a nonlinear behavior similar to the previous one, the training signal shown in Figure 20 is given as input to the ROM training algorithm. Its frequency content is similar to the one presented in Figure 11a. The signals root mean square is set to 0.125 for the plunge, 0.0625 radians for the pitch, 0.0125 radians for the leading edge control surface and 0.0250 radians for the trailing edge control surface degrees of freedom. The parameter ω_0 of the smoothing filter is set to obtain a cut-off reduced frequency of $k = 0.4$. As can be noticed from Figure 20b, the aerodynamic loads acting on the control surfaces are negligible compared to the lift and moment coefficients of the airfoil.

As for the previous case, the ROM nonlinear performance is evaluated considering large amplitude structural input. The motion amplitude is set to $\bar{h}/c = 0.3$ for the plunge, $\bar{\theta} = 5$ deg for the pitch, $\bar{\beta}_{LE} = \bar{\beta}_{TE} = 8$ deg for the leading and trailing edge degrees of freedom, all much greater than the maximum amplitude excited by the training signal shown in Figure 20. The excitation frequency is set to $k = 0.7$. Attention is focused again on the moment coefficient, because it is the one characterized by the strongest nonlinear behavior. Figure 21 depicts a close-up near the FFT peaks of the computed response. It can be noticed that as the number of states is increased, the ROM response gets closer to the reference solution. Therefore, also in this case the ROM shows good accuracy in predicting nonlinear unsteady aerodynamic loads, even when both amplitude and frequency of the input signal are beyond the limits considered during the training.

Coupling then the aerodynamic reduced order model with the structural model it is possible to reproduce

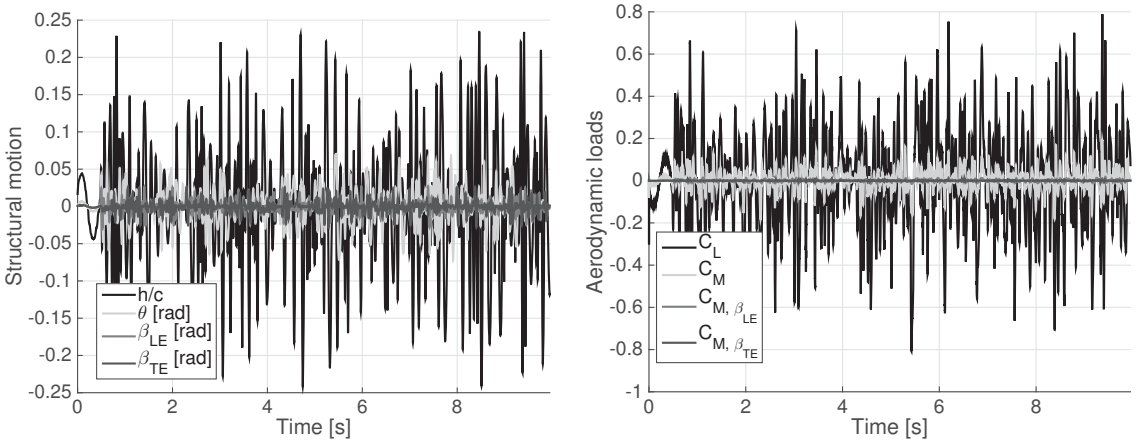

(a) Input: structural motion. **(b)** Output: aerodynamic loads.

Figure 20: Training signal for the four degree-of-freedom typical section.

nonlinear aeroelastic responses. A convergence analysis is again performed considering the value of the bifurcation point computed by the CFD code as a target. Such a value results in $V_{\text{bif}} = 0.635$, being slightly different with respect to the previous test case. In Fig. 22a such a convergence test is presented graphically. In this case, the training signal is 10 seconds long, which proved to be sufficient in the previous section. The average training time is 6 hours, considerably longer than the 2 degree-of-freedom case, because of the

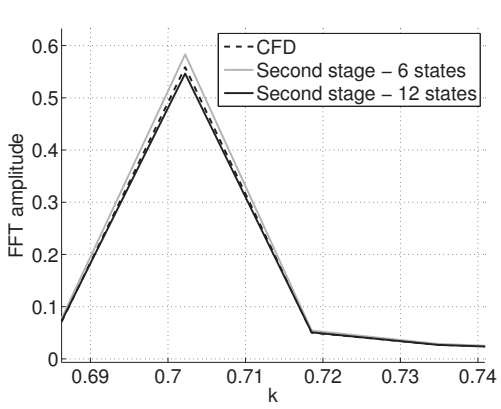

(a) Close-up near the first harmonic response peak.

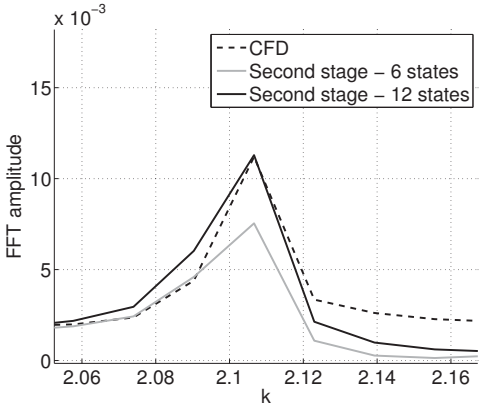

(b) Close-up near the third harmonic response peak.

Figure 21: Moment coefficient FFT for large structural motion, four degree-of-freedom case.

increased size of the input-output data pair vectors. Also, note the smoothness of the present convergence analysis, much more evident than for the previous test case. A sample of ROM-based aeroelastic V-g diagram is shown in Fig. 22b, where it is clear that the two control surfaces are only lightly influenced by the aerodynamic forces compared to the pitch and plunge degrees of freedom. A zoom near the flutter point is provided to make clearer the instability mechanism, which resembles the classical plunge-pitch flutter [30].

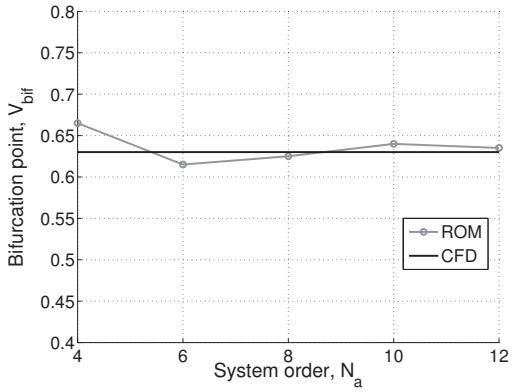

(a) Convergence analysis based on the bifurcation point.

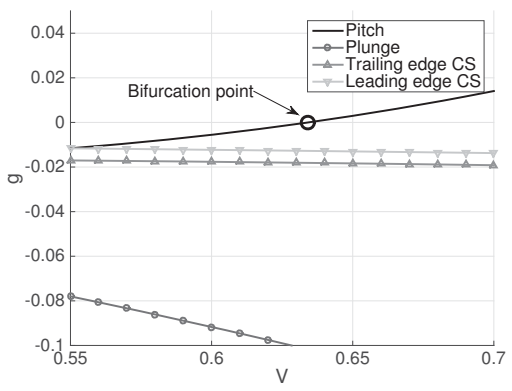

(b) Aeroelastic V-g diagram, $N_a = 12$.

Figure 22: Stability properties of the linearized system.

A comparison between the CFD and a 12 states ROM-based simulation at $V = 0.74$ is presented in Fig. 23. As it can be seen, the difference between the two results is quite small, showing that the reduced order model is able to capture the basic nonlinear features of the response. It is also possible to perform trend analyses to understand how the variations in flight speed influence the limit cycle oscillation amplitude and frequency. The results are shown in Fig. 24 and 25, where the outcomes of the ROM of ref. [14] are also presented. It is evident from Fig. 24 that increasing the number of states lead to a better correlation between

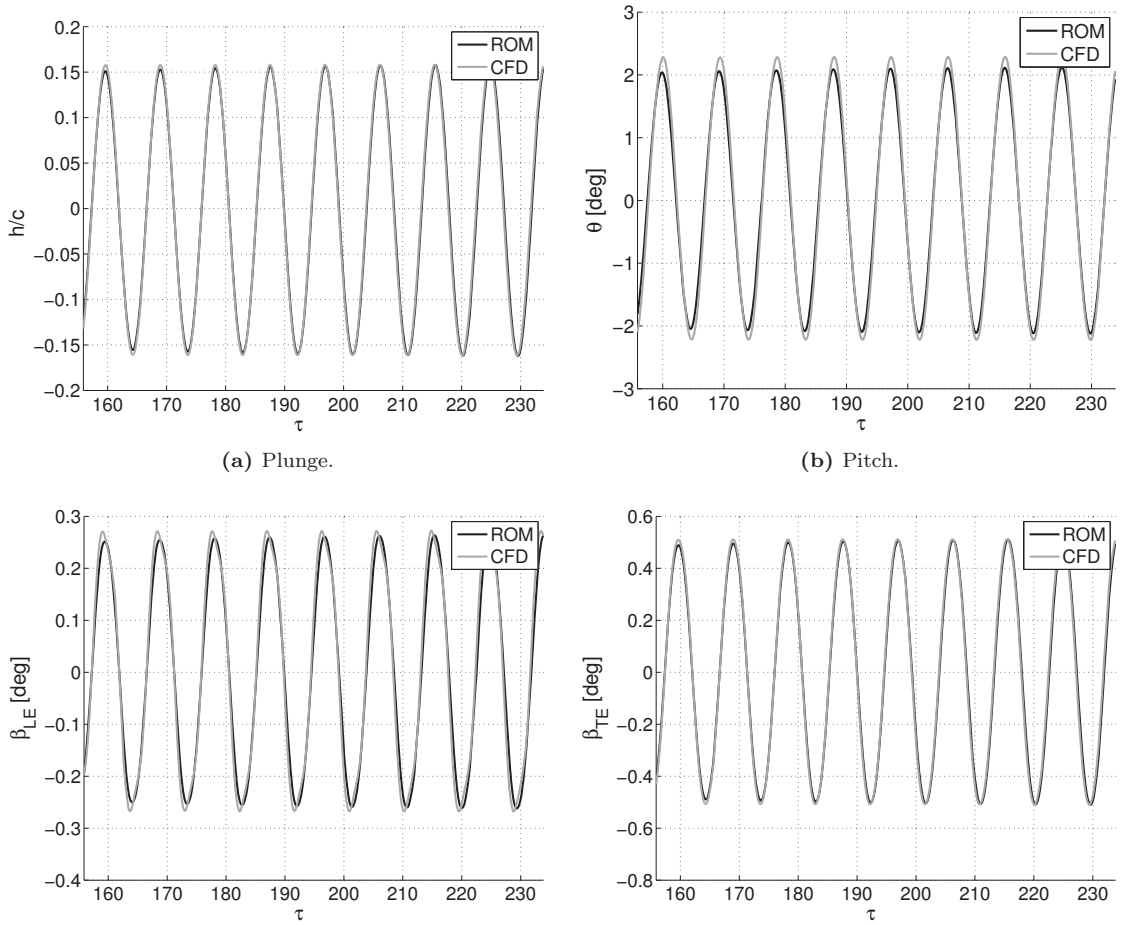

(a) Plunge.

(b) Pitch.

(c) Leading edge deflection.

(d) Trailing edge deflection.

Figure 23: Comparison between CFD and ROM-based aeroelastic simulations, $V = 0.74$, $N_a = 12$.

CFD and ROM-based results. However, it is interesting to note that the results with $N_a = 6$ present the same trend of the CFD, slightly shifted to the left. Instead, the results with $N_a = 12$, even if showing a smaller overall error, exhibit a local trend slope quite different from the reference data. From a design point of view, the results obtained with $N_a = 6$ would be preferred, because they are conservative (they exhibit a lower bifurcation speed) and depict the same shape of the reference curve as well. Such differences may be considered as irrelevant, since all the reduced order models capture the essential features of the system behavior. However, the ROM with $N_a = 12$ produces the best estimation of the bifurcation point, predicted to be $V_{\text{bif}} = 0.64$, and also a more accurate prediction of the LCO frequency. Considering only the linear part of the same model, the computed bifurcation speed is $V_{\text{bif}} = 0.647$, therefore proving that the assumptions of Section II.A are valid in this case also. The ROM of ref. [14] presents qualitatively the same behavior of the ROM with $N_a = 12$, always overestimating both LCO amplitude and frequency. Such a ROM is characterized by the following parameters: $n_x = 8$ and $n_h = 10$, for the details please see [14].

As a final result, in Table 3 is reported a comparison in terms of the time required to compute the previous

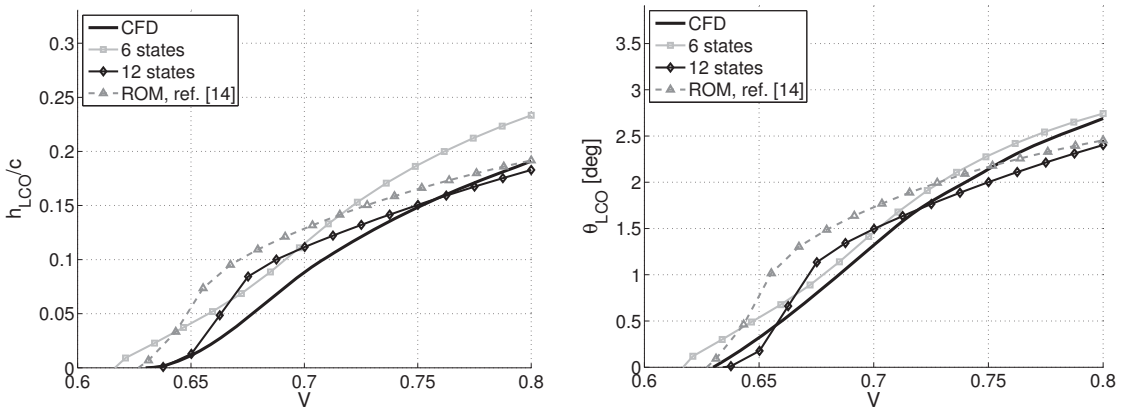

(a) Plunge trend. **(b)** Pitch trend.

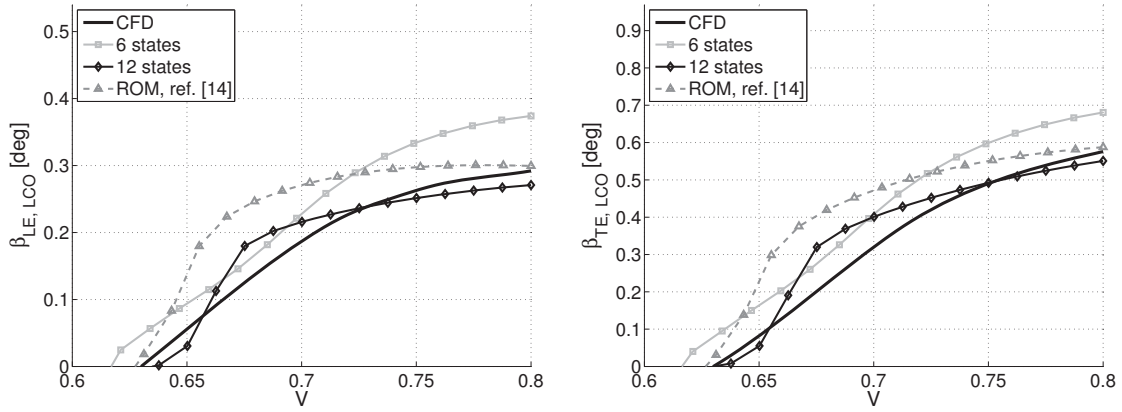

(c) Leading edge deflection trend. **(d)** Trailing edge deflection trend.

Figure 24: LCO amplitude trends comparison.

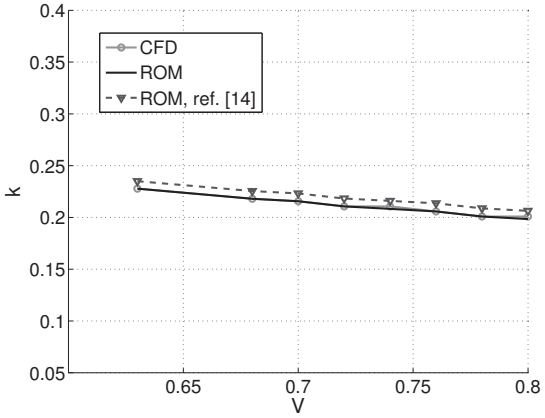

Figure 25: LCO frequency trends comparison between CFD and 12 states ROM-based simulations.

LCO trends. The time savings is still substantial, confirming again the convenience of developing ROMs from the more expensive simulations, especially in the case when optimization analyses or control law designs have to be performed. Note that even if in this case the ratio between the two total times is about 3.5, such

a result would greatly improve as the number of analyses to be carried out is increased. As before, the ROM of ref. [14] requires a longer training time, and the same conclusions drawn in the previous case are still valid.

	CFD	ROM	ROM, ref. [14]
Training signal generation, hours	-	12	12
Training stage, hours	-	6	9
Trend calculation, hours	10×7 points	0.0028×15 points	0.0023×15 points
	70	0.042	0.0345
Total, hours	70	18.042	21.0345

Table 3: Computational time required for computing the LCO trends, 4 degree-of-freedom typical section.

IV. Concluding Remarks

This effort has detailed the development of nonlinear aerodynamic reduced order models, built upon input-output data generated by Euler based CFD simulations. The problem is formulated in the continuous time domain, making it possible to vary the integration time step. This has led to a speed-up in the reduced order model simulations, while demonstrating good robustness given large variations of the time step. This feature could also be exploited in the design of control laws, where the determination of an appropriate sampling time is often of great importance. Two test cases were considered, showing the ability of the proposed approach to deal with an increasing number of degrees of freedom, in both aerodynamic and aeroelastic applications. Furthermore, several high fidelity CFD analyses were performed to fully understand the mechanism behind aerodynamically induced limit cycle oscillations. The efficiency of the presented ROM procedure has the potential of making possible a more extensive adoption of nonlinear aeroelastic analyses in the early stages of aircraft design, while maintaining adequate accuracy in comparison to the costlier traditional CFD calculations.

A. Computation of the sensitivities terms $\mathbf{x}_{\mathbf{a}_{/\mathbf{p}}}$ and $\mathbf{f}_{\mathbf{a}_{/\mathbf{p}}}$

As reported in Sec. II.A, the system of differential equations represented by Eq. 3 has to be solved at each LM iteration. Here we provide the analytical definition of all the terms governing the dynamics of $\mathbf{x}_{\mathrm{a}_{/\mathbf{p}}}$. Calling $\mathrm{vec}\,(\cdot)$ the operator which stacks the column of a matrix in a vector, we can define the optimization

unknown as $\mathbf{p} = \left\{ \mathrm{vec}\left(\mathbf{E}_\mathrm{a}\right)^\mathrm{T}, \mathrm{vec}\left(\mathbf{F}_\mathrm{a}\right)^\mathrm{T} \right\}^\mathrm{T}$. The sensitivity term $\dot{\mathbf{x}}_{\mathrm{a}_{/\mathbf{p}}}$ is then computed as:

$$\dot{\mathbf{x}}_{a/E_{ij}} = \left(\mathbf{A}_\mathrm{a} + \mathbf{E}_\mathrm{a}\boldsymbol{\Phi}\left(\mathbf{x}_\mathrm{a}\right)\right)\mathbf{x}_{a/E_{ij}} + \mathbf{I}_{ij}\boldsymbol{\phi}\left(\mathbf{x}_\mathrm{a}\right) \qquad i,j = 1,\dots,N_a \tag{8a}$$

$$\dot{\mathbf{x}}_{a/F_{ij}} = \left(\mathbf{A}_\mathrm{a} + \mathbf{E}_\mathrm{a}\boldsymbol{\Phi}\left(\mathbf{x}_\mathrm{a}\right)\right)\mathbf{x}_{a/F_{ij}} \qquad i = 1,\dots,N_\mathrm{out},\ j = 1,\dots,N_a \tag{8b}$$

$$\dot{\mathbf{x}}_{\mathrm{a}_{/\mathbf{p}}} = \left(\mathbf{A}_\mathrm{a} + \mathbf{E}_\mathrm{a}\boldsymbol{\Phi}\left(\mathbf{x}_\mathrm{a}\right)\right)\mathbf{x}_{\mathrm{a}_{/\mathbf{p}}} + \mathbf{U}_\mathbf{x} \tag{8c}$$

where $\boldsymbol{\Phi}\left(\mathbf{x}_\mathrm{a}\right) = \mathrm{Diag}\left(\phi'\left(x_{a,1}\right), \phi'\left(x_{a,2}\right), \dots, \phi'\left(x_{a,N_a}\right)\right)$, being $\phi'\left(\cdot\right)$ the first derivative of $\phi\left(\cdot\right)$ with respect to its argument, while matrix $\mathbf{U}_\mathbf{x}$ is so defined:

$$\mathbf{U}_\mathbf{x} = \left[\phi\left(x_{a,1}\right)\mathbf{I}_{N_a}, \phi\left(x_{a,2}\right)\mathbf{I}_{N_a}, \cdots \mid \phi\left(x_{a,N_a}\right)\mathbf{I}_{N_a}, \mathbf{0}, \cdots, \mathbf{0}\right] \tag{9}$$

being $\mathbf{I}_{N_a}$ the identity matrix of size N_a.

In order to assemble the Jacobian matrix of Eq. 4, the sensitivity term $\mathbf{f}_{\mathrm{a}_{/\mathbf{p}}}$ has to be computed as well. This can be performed similarly to Eqs. 8:

$$\mathbf{f}_{a/E_{ij}}/q_\infty = \left(\mathbf{C}_\mathrm{a} + \mathbf{F}_\mathrm{a}\boldsymbol{\Phi}\left(\mathbf{x}_\mathrm{a}\right)\right)\mathbf{x}_{a/E_{ij}} \qquad i,j = 1,\dots,N_a \tag{10a}$$

$$\mathbf{f}_{a/F_{ij}}/q_\infty = \left(\mathbf{C}_\mathrm{a} + \mathbf{F}_\mathrm{a}\boldsymbol{\Phi}\left(\mathbf{x}_\mathrm{a}\right)\right)\mathbf{x}_{a/F_{ij}} + \mathbf{I}_{ij}\boldsymbol{\phi}\left(\mathbf{x}_\mathrm{a}\right) \qquad i = 1,\dots,N_\mathrm{out},\ j = 1,\dots,N_a \tag{10b}$$

$$\mathbf{f}_{\mathrm{a}_{/\mathbf{p}}}/q_\infty = \left(\mathbf{C}_\mathrm{a} + \mathbf{F}_\mathrm{a}\boldsymbol{\Phi}\left(\mathbf{x}_\mathrm{a}\right)\right)\mathbf{x}_{\mathrm{a}_{/\mathbf{p}}} + \mathbf{U}_{\mathbf{f}_a} \tag{10c}$$

where matrix $\mathbf{U}_{\mathbf{f}_a}$ is so defined:

$$\mathbf{U}_{\mathbf{f}_a} = \left[\mathbf{0}, \cdots, \mathbf{0}, \phi\left(x_{a,1}\right)\mathbf{I}_{N_\mathrm{out}}, \phi\left(x_{a,2}\right)\mathbf{I}_{N_\mathrm{out}}, \cdots, \phi\left(x_{a,N_a}\right)\mathbf{I}_{N_\mathrm{out}}\right] \tag{11}$$

Acknowledgments

The authors would like to thank Prof. Paolo Mantegazza of Politecnico di Milano for his constant advice and support.

References

[1] B.N. Bond, Z. Mahmood, Yan Li, R. Sredojevic, A. Megretski, V. Stojanovi, Y. Avniel, and L. Daniel. Compact modeling of nonlinear analog circuits using system identification via semidefinite programming and incremental stability certification. *IEEE Transactions on Computer-Aided Design of Integrated Circuits and Systems*, 29(8):1149–1162, Aug 2010.

[2] M.I. Younis, E.M. Abdel-Rahman, and A. Nayfeh. A reduced-order model for electrically actuated microbeam-based mems. *Journal of Microelectromechanical Systems*, 12(5):672–680, Oct 2003.

[3] D. Amsallem, J. Cortial, K. Carlberg, and C. Farhat. A method for interpolating on manifolds structural dynamics

reduced-order models. *International Journal for Numerical Methods in Engineering*, 80(9):1241–1258, 2009.

[4] D. J. Lucia, P. S. Beran, and W. A. Silva. Reduced-order modeling: new approaches for computational physics. *Progress in Aerospace Sciences*, 40:51–117, 2004.

[5] K.C. Hall, J. Thomas, and E. Dowell. Proper Orthogonal Decomposition Technique for Transonic Unsteady Aerodynamic Flows. *AIAA Journal*, 38:1853–1862, 2000.

[6] J. P. Thomas, E. H. Dowell, and K. C. Hall. Nonlinear inviscid aerodynamic effects on transonic divergence, flutter, and limit-cycle oscillations. *AIAA Journal*, 40:638–646, 2002.

[7] G. Chen, Y. Li, and G. Yan. Nonlinear POD Reduced Order Model for Limit Cycle Oscillation Prediction. *Science China Physics, Mechanics and Astronomy*, 53, Issue 7:1325–1332, 2010.

[8] S. Timme, S. Marques, and Badcock K. J. Transonic aeroelastic stability analysis using a Kriging-based Schur complement formulation. *AIAA Journal*, 49:1202 – 1213, 2011.

[9] S. Timme and J. K. Badcock. Transonic aeroelastic instability searches using sampling and aerodynamic model hierarchy. *AIAA Journal*, 49:1191 – 1201, 2011.

[10] M. Balajewicz and E. Dowell. Reduced-Order Modeling of Flutter and Limit-Cycle Oscillations Using the Sparse Volterra Series. *Journal Of Aircraft*, 49:1803–1812, 2012.

[11] W. Silva. Identification of Nonlinear Aeroelastic Systems Based on the Volterra Theory: Progress and Opportunities. *Nonlinear Dynamics*, 39:25–62, 2005.

[12] C. M. Denegri and M. R. Johnson. Limit cycle oscillation prediction using artificial neural networks. *Journal of Guidance, Control, and Dynamics*, 24(5):887–895, 2014/06/20 2001.

[13] K. Lindhorst, M.C. Haupt, and P. Horst. Nonlinear reduced order modeling for aeroelastic simulation with neural networks. In Norbert Kroll, Rolf Radespiel, Jan Willem Burg, and Kaare Sørensen, editors, *Computational Flight Testing*, volume 123 of *Notes on Numerical Fluid Mechanics and Multidisciplinary Design*, pages 131–149. Springer Berlin Heidelberg, 2013.

[14] A. Mannarino and P. Mantegazza. Nonlinear aeroelastic reduced order modeling by recurrent neural networks. *Journal of Fluids and Structures*, 48(0):103 – 121, 2014.

[15] B. Glaz, L. Liu, and P. P. Friedmann. Reduced-order nonlinear unsteady aerodynamic modeling using a surrogate-based recurrence framework. *AIAA Journal*, 48(10):2418–2429, 2014/06/20 2010.

[16] D. E. Raveh. Reduced-Order Models for Nonlinear Unsteady Aerodynamics. *AIAA Journal*, 39(8):1417–1429, 2001.

[17] S. Haykin. *Neural Networks and Learning Machines*. Prentice Hall, Upper Saddle River, NJ; 3 edition, 2008.

[18] M. Spiker, J. P. Thomas, K. C. Hall, R. Kielb, and E. H. Dowell. Modeling cylinder flow vortex shedding with enforced motion using a harmonic balance approach. *47th AIAA/ASME/ASCE/AHS/ASC Structures, Structural Dynamics, and Materials Conference, AIAA paper 2006-1965*, 2006.

[19] W. Yao and M. Liou. Reduced-order modeling for flutter/LCO using recurrent artificial neural network. In *12th AIAA Aviation Technology, Integration, and Operations (ATIO) Conference and 14th AIAA/ISSM, Indianapolis, IN*, 2012.

[20] P. Van Overschee and B. De Moor. N4SID: Subspace algorithms for the identification of combined deterministic-stochastic systems. *Automatica*, 30(1):75 – 93, 1994. Special issue on statistical signal processing and control.

[21] D. Marquardt. An algorithm for least-squares estimation of nonlinear parameters. *Journal of the Society for Industrial and Applied Mathematics*, 11(2):431–441, 1963.

[22] M.D. Conner, D.M. Tang, E.H. Dowell, and L. N. Virgin. Nonlinear behavior of a typical airfoil section with control surface freeplay: A numerical and experimental study. *Journal of Fluids and Structures*, 11(1):89–109, 1997.

[23] W. A. Silva. Reduced-order models based on linear and nonlinear aerodynamic impulse responses. Technical report, NASA, 1999.

[24] G Romanelli, E. Serioli, and P. Mantegazza. A "Free" Approach to Computational Aeroelasticity. In *48th AIAA Aerospace Sciences Meeting and Exhibit, Orlando, FL*, 2010.

[25] G. Romanelli, M. Castellani, P. Mantegazza, and S. Ricci. Coupled CSD/CFD non-linear aeroelastic trim of free-flying flexible aircraft. In *53rd AIAA/ASME/ASCE/AHS/ASC Structures, Structural Dynamics and Materials Conference, Honolulu, HI*, 2012.

[26] E. H Dowell, R. Clark, D. Cox, H. C. Curtiss Jr., J. W. Edwards, K. C. Hall, D. A. Peters, R. Scanlan, E. Simiu, F. Sisto, and T. W. Strganac. *A Modern Course In Aeroelasticity, 4th Edition, Chapter 11.* Kluver Academic Publishers, Berlin, Germany, 2004.

[27] P. Masarati, M. Lanz, and P. Mantegazza. Multistep integration of ordinary, stiff, and differential-algebraic problems for multibody dynamics applications. In *XVI Congresso nazionale AIDAA, Palermo, Italy*, 2001.

[28] V. Mukhopadhyay. Transonic Flutter Suppression Control Law Design and Wind-Tunnel Test Results. *Journal Of Guidance, Control and Dynamics*, 23:930–937, 2000.

[29] A. Mannarino and P. Mantegazza. Multifidelity control of aeroelastic systems: An immersion and invariance approach. *Journal of Guidance, Control, and Dynamics*, 37(5):1568–1582, 2014.

[30] R. L. Bisplinghoff, H. Ashley, and R. L. Halfman. *Aeroelasticity, Chapter 9.* Dover, New York, NY, 1955.